



Improved coulombic efficiency in nanocomposite thin film based on electrodeposited-oxidized FeNi-electrodes for lithium-ion batteries

María C. López, Gregorio F. Ortiz*, Pedro Lavela, Ricardo Alcántara, José L. Tirado

Laboratorio de Química Inorgánica, Universidad de Córdoba, Edificio Marie Curie, Campus de Rabanales, 14071 Córdoba, Spain

ARTICLE INFO

Article history:

Received 4 September 2012

Received in revised form 14 November 2012

Accepted 28 December 2012

Available online 7 January 2013

Keywords:

Energy storage materials

Cell polarization

Thin film electrodes

Lithium batteries

Iron and nickel oxide electrodes

ABSTRACT

Electrochemical deposition from Ni^{2+} and Fe^{2+} using sulfate and nitrate solutions is carried out under galvanostatic regime. The resulting films are oxidized and examined in lithium test cells as potential anode materials for lithium-ion batteries. X-ray diffraction, XPS and SAED-TEM analyses revealed a thin film based on nanocomposite NiO and Fe_2O_3 . Cycling studies show the smallest discharge polarization ever reported during the conversion reactions of metal oxides at ~ 0.8 V. Unlike typical transition metal oxides, the amorphous oxidized material exhibited low irreversibility from first to second discharge ($\sim 15\%$) and a distinctive plateau on consecutive discharge branches. The changes in the film thickness on increasing deposition time and the crystallization phenomena on annealing the deposits strongly affect the electrochemical behavior. The present approach allows preparing a powder free electrode with improved coulombic efficiency directly on the current collector and opens a set of novel preparation routes in this field with intriguing results.

© 2013 Elsevier B.V. All rights reserved.

1. Introduction

The last few years have seen renewed interest in solid state batteries. Two examples are Planar Energy Company in Florida, and its solid-state lithium-ion battery design that can deliver three times the energy density of earlier lithium-ion batteries at less than half the cost per kilowatt-hour [1]; and Toyota, that in partnership with academic researchers have recently developed a prototype solid-state battery [2]. Since the battery can easily be processed into sheet form, it can store several times the amount of electricity, volume for volume, than the current generation of electric vehicle batteries, according to the developers. This added capacity may extend the maximum driving distance per charge for compact EVs to around 1000 km [621 miles] from the 200 km or so for existing vehicles.

Electrode materials for all-solid-state batteries can be prepared by electrochemical procedures. The advantages of electrochemical preparation routes include: (i) film formation onto current collector; (ii) control over layer thickness and active material, (iii) effective packing of electroactive materials, (iv) multilayer deposits without separator, (v) additives (binder or conductive) are avoided, and (vi) good contact with the electrolyte is assured. Experimental procedures to obtain the electrode material films can be found among anodization and electrochemical deposition techniques.

* Corresponding author. Tel./fax: +34 957 21 86 37.

E-mail address: q72maorg@uco.es (G.F. Ortiz).

Recently, we studied the use of TiO_2 nanotubes prepared by titanium anodization [3,4]. The resulting nanostructured electrodes showed enhanced lithium storage capacities per area unit, as compared with compact layers of the same material. In an attempt to further increase the capacity of the electrodes, composite materials were prepared by two different strategies. The first one was to combine nt-TiO_2 with SnO_x nanowires, which were electrodeposited on the freshly-prepared TiO_2 films. The resulting composite increased by a factor of two the initial capacity by a Li-Sn alloying mechanism [5]. A second strategy was found to be even more effective: electrodeposition of iron followed by mild oxidation to Fe_2O_3 , which acted as a conversion electrode material. The resulting reversible capacities were significantly larger than in the previous studies. However, these composite electrodes were penalized by a common factor affecting conversion electrode materials: A pronounced irreversibility of the first cycle, leading to poor coulombic efficiencies [6].

A completely new strategy was recently reported for $\text{Fe}-\text{Co}-\text{Ni}$ deposits, which avoided the use of titania substrate while showing high areal capacities and unexpectedly high coulombic efficiency in the first cycle. The method combined electrodeposition of the transition metal ions on the surface of clean titanium surfaces, followed by a mild thermal treatment to obtain the transition metal oxides. The resulting coulombic efficiency was ca. 85% [7]. In that communication, the mechanism causing the improved reversibility in the first cycle was left for further studies [8]. In addition, the use of cobalt in the composition posed the usual cost and environmental concerns.

In this work, new Fe–Ni oxides films are prepared and evaluated in lithium test cells. It is found that the coulombic efficiency is preserved in the absence of cobalt. Moreover, the origin of this unusual and interesting behavior is studied by a combination of electrochemical, X-ray and electron diffraction and spectroscopic techniques which provide different clues for the understanding of this behavior.

2. Experimental

For the preparation of FeNi deposits, stoichiometric amounts of iron(II) sulfate and nickel(II) nitrate (Fe:Ni = 1:1, conc.: 0.02 M) were dissolved in deionized water. The electrodeposition experiments were carried out at room temperature, using -5 mA cm^{-2} current density during two different periods of time: 240 and 1200 s. Programmable galvanostat/potentiostat PGSTAT12 Autolab and Arbin instruments with a glass reference electrode (Ag/AgCl) and a platinum wire as counter-electrode were used. The deposits were obtained on 170 μm -thick Ti foil (99.7% purity) and were used as working electrodes. In order to obtain the oxidized Fe–Ni materials for lithium test cells, the as-deposited films were treated at 450 °C in air for 2 h. Cyclic voltammetric experiments (at 10 mV s^{-1}) for deposition of single Fe^{2+} and Ni^{2+} ions and mixed Fe–Ni ions on Ti foils were carried out from the open circuit potential to -2.5 V , going first in the cathodic direction. For that purpose a PGSTAT302N instrument is used. The aqueous electrolytes contains 0.04 M $\text{Ni}(\text{NO}_3)_2 \cdot 6\text{H}_2\text{O}$, 0.04 M $\text{FeSO}_4 \cdot 7\text{H}_2\text{O}$, and a mixture of $\text{Ni}(\text{NO}_3)_2$ and $\text{FeSO}_4 \cdot 7\text{H}_2\text{O}$.

Grazing-Incidence Small-Angle X-ray Diffraction (GISAXRD) patterns were obtained in an EQ 31 04 Panalytical X'Pert PRO MPD system with $\text{Cu K}\alpha$ and $\text{Mo K}\alpha$ radiations. Scanning electron micrographs were obtained with a JEOL-SM6300 and transmission electron micrographs with a JEOL JEM 2100 instrument, respectively. Nitrogen adsorption–desorption isotherms were obtained with a Quantachrome-Nova instrument at 77 K. The sample was previously degassed under vacuum at 200 °C. The chemical state and compositions of electrode materials were analyzed using X-ray Photoelectron Spectroscopy (XPS, SPECS Phobos 150MCD) using $\text{Mg K}\alpha$ source and a chamber pressure of $4 \times 10^{-9} \text{ mbar}$.

The electrochemical study was performed using Arbin and Bio-Logic MPG-2 multichannel potentiostat/galvanostat systems. The cells were mounted in an argon-filled glove box with moisture and oxygen levels below 2 ppm. The cells can be summarized as $\text{Li}/1 \text{ M LiPF}_6$ (EC:DMC = 1:1 in mass ratio)/FeNi-based electrodes.

3. Results and discussion

The electrodeposition experiments on the surface of the titanium foil were followed by recording potential-time curves (Fig. 1A). The potential transients showed an abrupt decrease in voltage in less than one second (ca. 0.2 s), followed by an increase until a constant voltage value of ca. -1.15 V vs. Ag/AgCl was reached. The drop in voltage is indicative of an increase in the electroactive area, as the number of nuclei increases and/or the independent nuclei grow in size. The constant region occurs when nucleation and growth processes have taken place. The Faraday's law showed contents of 0.35 and 1.8 mg cm^{-2} of metal oxides in the films prepared by 240 and 1200 s experiments, respectively. In order to have accurate electrode material mass, ICP analyses of the oxidized films were performed. For that purpose, the deposits were dissolved with 1 mL of HNO_3 and 3 mL of HCl heating at 75 °C during few minutes and then rinsed with distilled water until a total volume of 100 mL. The ICP confirmed the presence of 0.30 (0.13 mg cm^{-2} for NiO and 0.17 mg cm^{-2} for Fe_2O_3) and 1.33 mg cm^{-2} (0.54 mg cm^{-2} for NiO and 0.79 mg cm^{-2} Fe_2O_3) of metal oxides for the thin films prepared during 240 and 1200 s, respectively. Deposits film can reach as much as 5 μm thick for 1200 s of deposition (insets Fig. 1), five times higher than for short time (1 μm), with a similar rough texture and with numerous orderly nanosheets interconnected between them and forming a microporous structure. EDX measurements showed a 1:1:Fe:Ni ratio in both samples (Fig. 1, inset). These ratios are in contradiction with the fact that each metal has a characteristic reduction potential. Nickel is nobler than iron and is expected to be reduced more easily (normal co-deposition). However, anomalous co-deposition is a phenomenon commonly found in the electroplating of alloys containing iron and other metals, such as nickel or cobalt

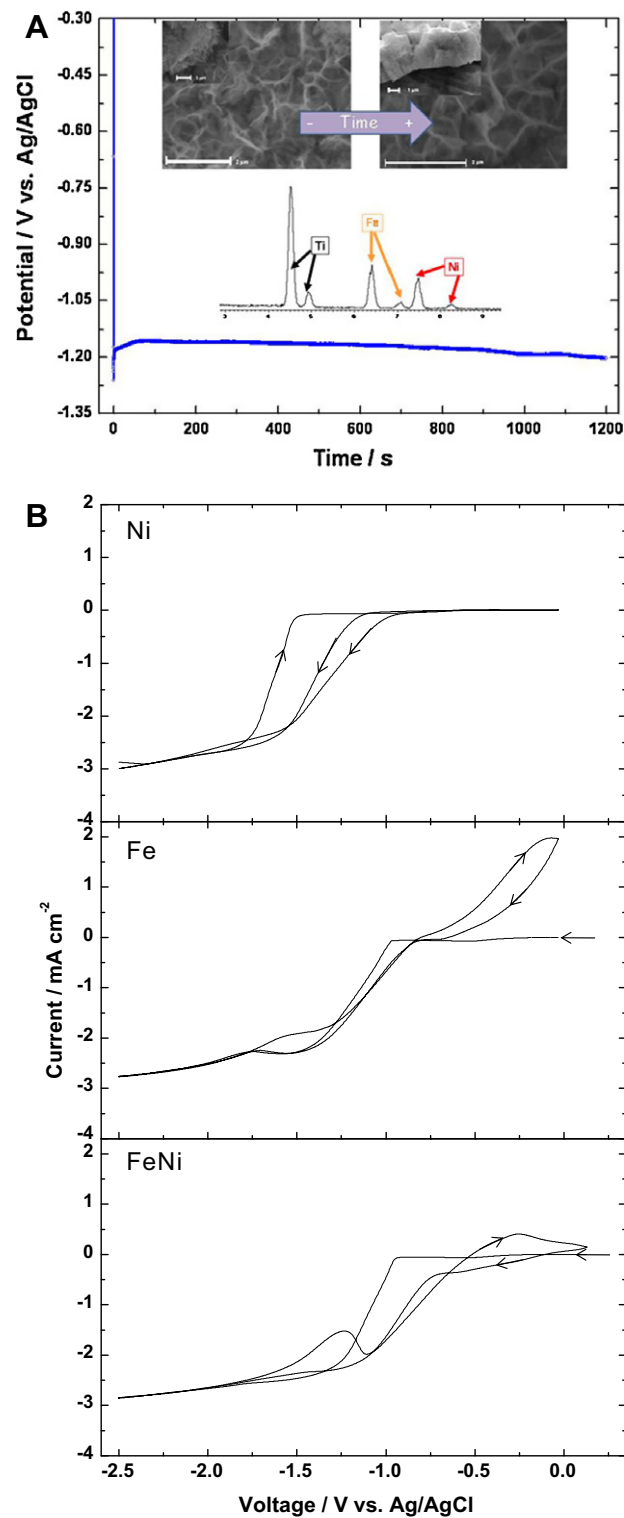


Fig. 1. (A) Potential vs. time curve recorded during the process of co-deposition of the binary FeNi alloy at -5 mA cm^{-2} . Insets: Energy dispersive X-ray analysis and SEM images of the film (for 240 and 1200 s of deposition time). (B) The cyclic voltammograms recorded at the sweep rate of 10 mV s^{-1} in the electrolytes containing 0.04 M $\text{Ni}(\text{NO}_3)_2 \cdot 6\text{H}_2\text{O}$, 0.04 M $\text{FeSO}_4 \cdot 7\text{H}_2\text{O}$, and a mixture of $\text{Ni}(\text{NO}_3)_2$ and $\text{FeSO}_4 \cdot 7\text{H}_2\text{O}$.

[9–11]. Thus, it was found that the Fe^{2+} ions are reduced and incorporated to the substrate together with Ni^{2+} ions, as the reduction of the less noble metal ions is a catalyzed process. Cyclic voltammetric experiments (at 10 mV s^{-1} sweep rate) for deposition of single Fe^{2+} and Ni^{2+} ions and mixed Fe^{2+} , Ni^{2+} ions on Ti foils were carried

out from the open circuit potential to a potential cathodic limit of -2.5 V, and anodic limit of 0.0 V vs. Ag/AgCl (Fig. 1b). During the first cathodic sweep, there was no reaction until ca. -1.0 V, in agreement with the initial oxidation state of the transition metals. Then deposition starts with an increase of the cathodic current taking place at -1.17 , -1.10 and -1.0 V (vs. Ag/AgCl) that is attributed to the nucleation and growth of Ni, Fe and mixed Fe–Ni. However, it should be noted that Fe^{2+} and Ni^{2+} ion deposition occurs by the reduction of these species with simultaneous hydrogen evolution which must be pronounced at potentials more negative than -1.3 V. Due to the concomitant pH increase in the vicinity of the electrode surface due to massive hydrogen evolution, it is possible that M^{2+} ions react with OH^- ions forming hydroxides or hydrated oxides which precipitate and prevent further deposition of metal powders [12]. This would explain that what we describe as anomalous co-deposition is in fact a complex phenomenon including hydroxide precipitates. It should be remarked that the as-prepared deposits do not show interesting electrochemical performance in lithium test cells. Thus they are only intermediates to the annealed films which are characterized below in more detail.

During the thermal treatment at 450 °C, the FeNi deposits were oxidized. The presence of the oxide products is confirmed below by TEM, GISAXRD, XPS and the electrochemical reaction with lithium. The high-resolution TEM (HRTEM) images in Fig. 2 reveal that the structure of the material deposited for 240 s is comprised of very few nano-crystallites with grain size ranging between 5 and 10 nm. Lattice fringes were only visible in a reduced number of regions in the sample, indicating that this material is not completely amorphous, but neither highly crystalline in nature (Fig. 2). The corresponding electron diffraction pattern in Fig. 2 reveals Debye circles ascribable to (104) and (110) reflections of $\alpha\text{-Fe}_2\text{O}_3$ and

(012) and (110) reflections of NiO, in good agreement with the results discussed below. Reflections ascribable to the titanium (JPDS # 05-0682) current collector were clearly detected in the GISAXRD patterns (Fig. 2). Also, with the aid of GISAXRD measurements, it was possible to study more accurately the thin film deposits than with standard XRD. Thus, the pattern corresponding to the oxidized thin films exhibits broad and low intensity peaks located around 33.2° , 35.6° and 62.6° (2θ), corresponding to the (104), (110) and (214) reflections of Fe_2O_3 (hematite, JPDS # 33-0664), and peaks at 37.3° , 43.2° , and 62.9° (2θ), corresponding to (101), (012) and (110) reflections of NiO (JPDS # 44-1159). When using Molybdenum radiation additional (202) reflection of $\alpha\text{-Fe}_2\text{O}_3$ ($d = 2.079$ Å) is detected as well as the (012) reflection of NiO phase (Fig. 2). Therefore, an inherent advantage of the electrochemical deposition technique is the suitable control of the amount, crystallinity and phases of the electrodeposited species.

XPS measurements were performed to better understand the chemical composition of FeNi-based thin films. Fig. 3 shows XPS spectra measured of oxidized FeNi alloy film at 450 °C before the reaction with lithium. The Fe 2p core levels are split into $2\text{p}_{1/2}$ and $2\text{p}_{3/2}$ components, due to the spin-orbit coupling. A signal at 711.4 eV of Fe^{3+} is clearly detected. As found in Fe_2O_3 -containing materials [13–15], the shake-up satellite line characteristic for the Fe^{3+} species is visible at 719 eV in Fig. 3. From the Ni 2p spectra in Fig. 3 the Ni $2\text{p}_{3/2}$ peak at 856 eV and Ni $2\text{p}_{1/2}$ peak at 873.4 eV entail the presence of Ni ions in the divalent state [16,17]. These results suggest that the composition of the whole film thickness is a mixture of Fe_2O_3 and NiO as suggested also by SAED–TEM and GISAXRD patterns.

The electrochemical conversion reactions of Transition Metal Oxides (TMOs) having rock-salt or spinel-type structures are well

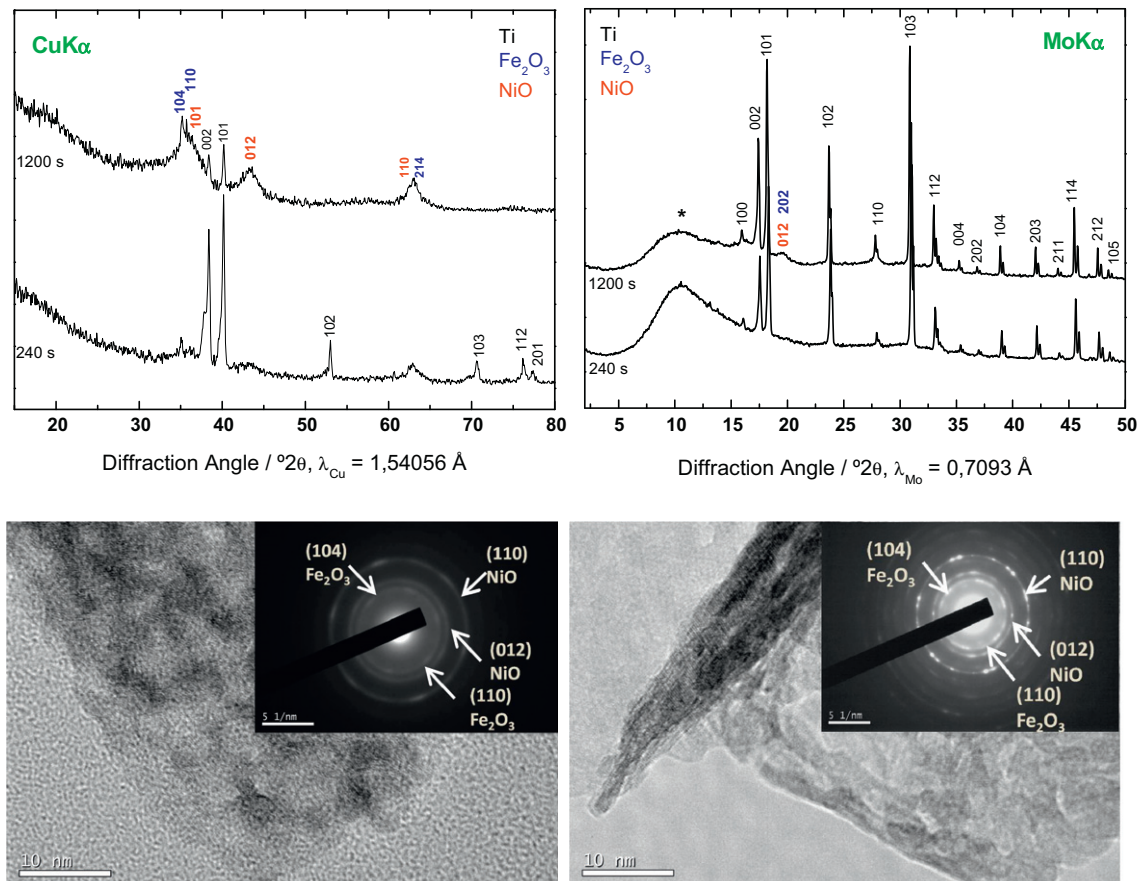


Fig. 2. Upper: Cu K α and Mo K α GISAXRD and Lower: TEM images (HREM and SAED) of samples deposited 240 s (left) and 1200 s (right).

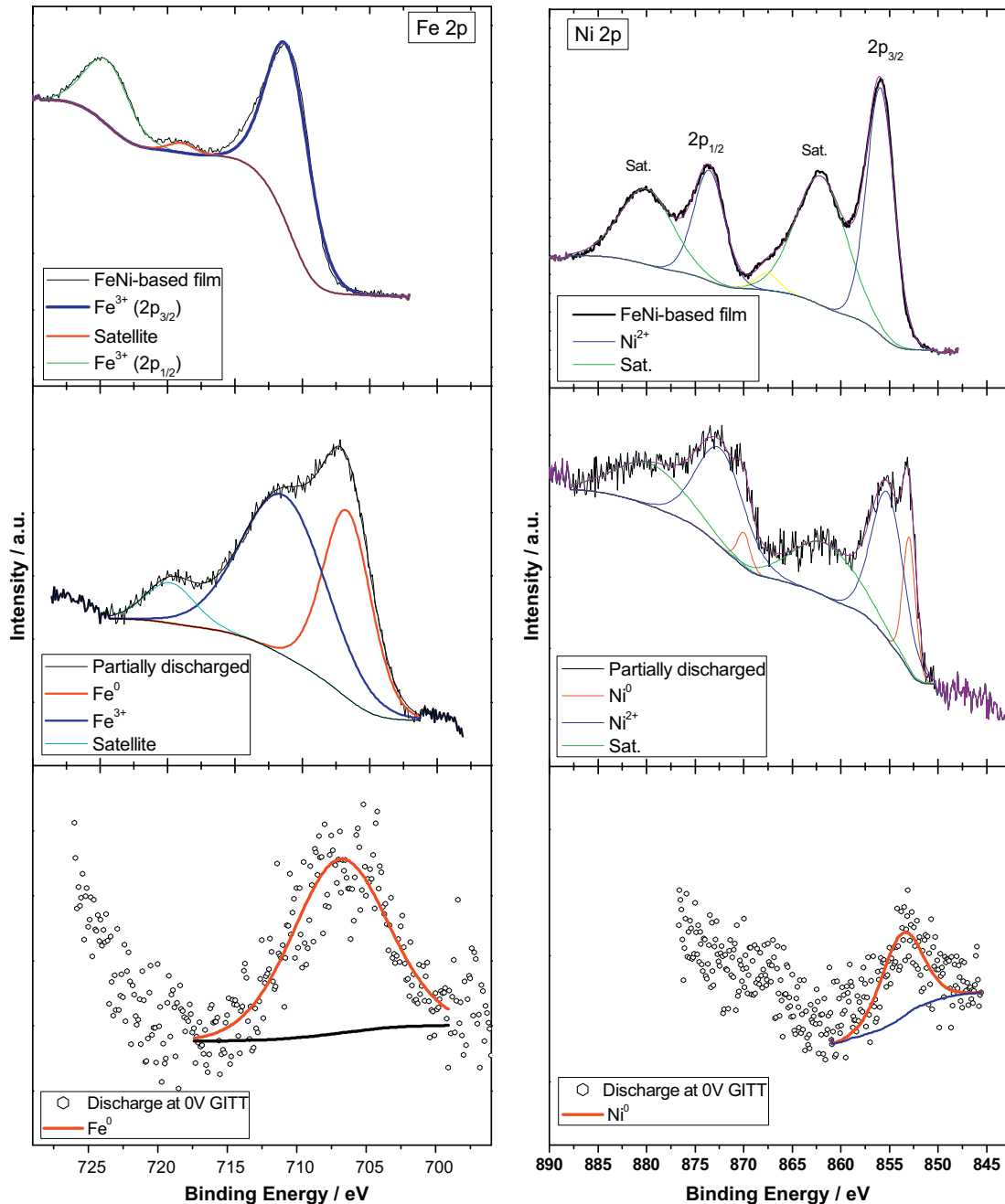


Fig. 3. XPS spectra of Fe 2p (left) and Ni 2p (right) for oxidized FeNi alloy at 450 °C prepared at short deposition times of 240 s (upper), after partial lithiation (middle) and discharged at 0 V (bottom) under GITT regime.

known [18–20]. The transition metal reduction is reflected in the galvanostatic curve of the first discharge by a plateau. The extent of this plateau matches fairly well with the number of electrons/mol required for the complete reduction of the transition metal to their metallic state [21,22]. In contrast to insertion reactions, the average voltage of the second discharge branch in conversion materials is significantly shifted to higher voltages, owing to the nanometric character of TMO particles reoxidized after the first charge against the pristine crystalline TMO [23–25]. Up to now, using nanocrystalline TMO powders as starting active materials for conversion reactions is known to result in superior kinetics and the accomplishment of high capacities at relatively high rates for an extended cycling [6,26]. However, the shift in cell potential and the irreversible capacity of the first cycle has not been greatly

reduced. A better control on these parameters by using an alternative approach in the preparation of the materials is the main objectives of this report.

The electrochemistry of the different materials prepared in this work is described in the next section by means of galvanostatic tests and their derivative curves (Fig. 4A and B). For comparison with electrodeposited-annealed FeNi-based electrode, the discharge and charge curves of electrodeposited-annealed pure Fe based electrode and electrodeposited-annealed pure Ni based electrode are provided. Their reversible capacities are 915 mA h g⁻¹ (or 220 μA h cm⁻²) and 620 mA h g⁻¹ (225 μA h cm⁻²), respectively (Table 1). In second discharge the potential of the reaction is shifted from 0.7 to 1.2 V for Ni-based electrode and from 0.8 to 1.0 V for Fe-based electrode (Fig. 4B). Their profiles are very similar

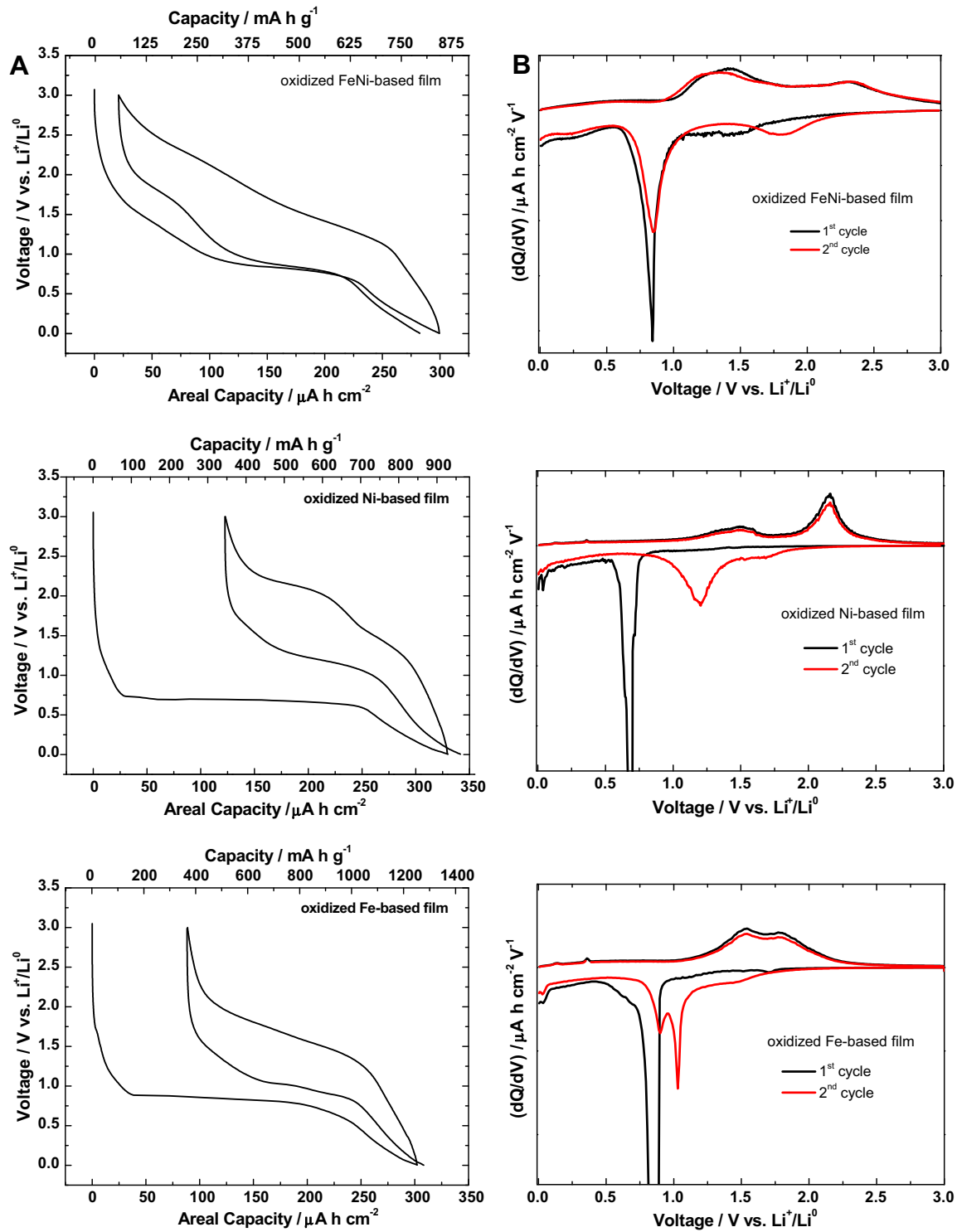


Fig. 4. (A) Galvanostatic discharge/charge curves of electrodeposited (240 s) and oxidized (450 °C): (upper) FeNi-based thin films, (middle) Ni-based thin film, and (bottom) Fe-based thin films. (B) Their corresponding derivative curves recorded from Li test cells. Cycling rate was 50 $\mu\text{A cm}^{-2}$ and voltage windows 0.01–3.0 V.

to those described in the above paragraph for crystalline solids. On the contrary, for the poorly-crystalline oxidized FeNi deposits (240 s), the mechanism of reaction with Li is far away from that observed in bulk crystalline metal oxides. Thus, no shifting in voltage from first to second discharge was observed because was kept invariable around 0.85 V. Moreover, the Li test cells showed a sloping voltage accounting for 100 $\mu\text{A h cm}^{-2}$ ($\sim 282 \text{ mA h g}^{-1}$) during the initial step of the first discharge (Fig. 4), which is followed by

a short quasi-plateau with around 125 $\mu\text{A h cm}^{-2}$ ($\sim 353 \text{ mA h g}^{-1}$). These features can be easily discerned in the derivative curves as a broadened signal at 1.5 V and a large peak at 0.8 V, and may be associated with electrolyte decomposition and reduction of Fe^{3+} and Ni^{2+} , respectively (Fig. 4). Eventually, a small reversible broadened band at 0.3 V reflects the formation of a polymeric gel-like layer and/or the accumulation of charge at the nanometric interphase between Li_2O and M^0 has been reported

Table 1

Values of theoretical capacity, first discharge capacity (include reversible and irreversible reactions) and efficiency from first to second cycle of different electrodes materials used in Li test cells.

Electrode	Th. capacity (mA h g ⁻¹)	1st Discharge capacity (mA h g ⁻¹)	Efficiency from 1st to 2nd cycle (%)	Reference data
NiO	717	800	78	Refs. [37,39]
		820	77	Refs. [38,40]
		930	65	Present work
Fe ₂ O ₃	1007	1575	77	Ref. [30]
		1210	58	Ref. [41]
		1254	71	Present work
FeNi-based material	615	843	85	Present work

by other authors [27,28]. Table 1 collects a list of capacities and first-cycle efficiencies found in the literature for different Ni and Fe-based electrodes, and compared with the materials reported here.

During the first charge, the profile of the derivative curve showed two broad and low intense bands placed at ca. 1.3 V and 2.3 V, ascribable to metal oxidation [29]. Unlike previous reports on high crystallinity TMO, the most interesting feature of the sec-

ond discharge is that the plateau ascribable to main reaction of metal reduction appears at the same voltage than that of the first discharge at 0.8 V (Fig. 4). Moreover, the signal at ca. 1.5 V disappears and a new band occurs at higher potential (ca. 1.8 V), which remains for successive cycles. This behavior is reproducible when the electrode material is cycled under potentiodynamic regime (see below). This behavior differs from those found in classical conversion reactions [18,20,30,31], and contributes to a higher revers-

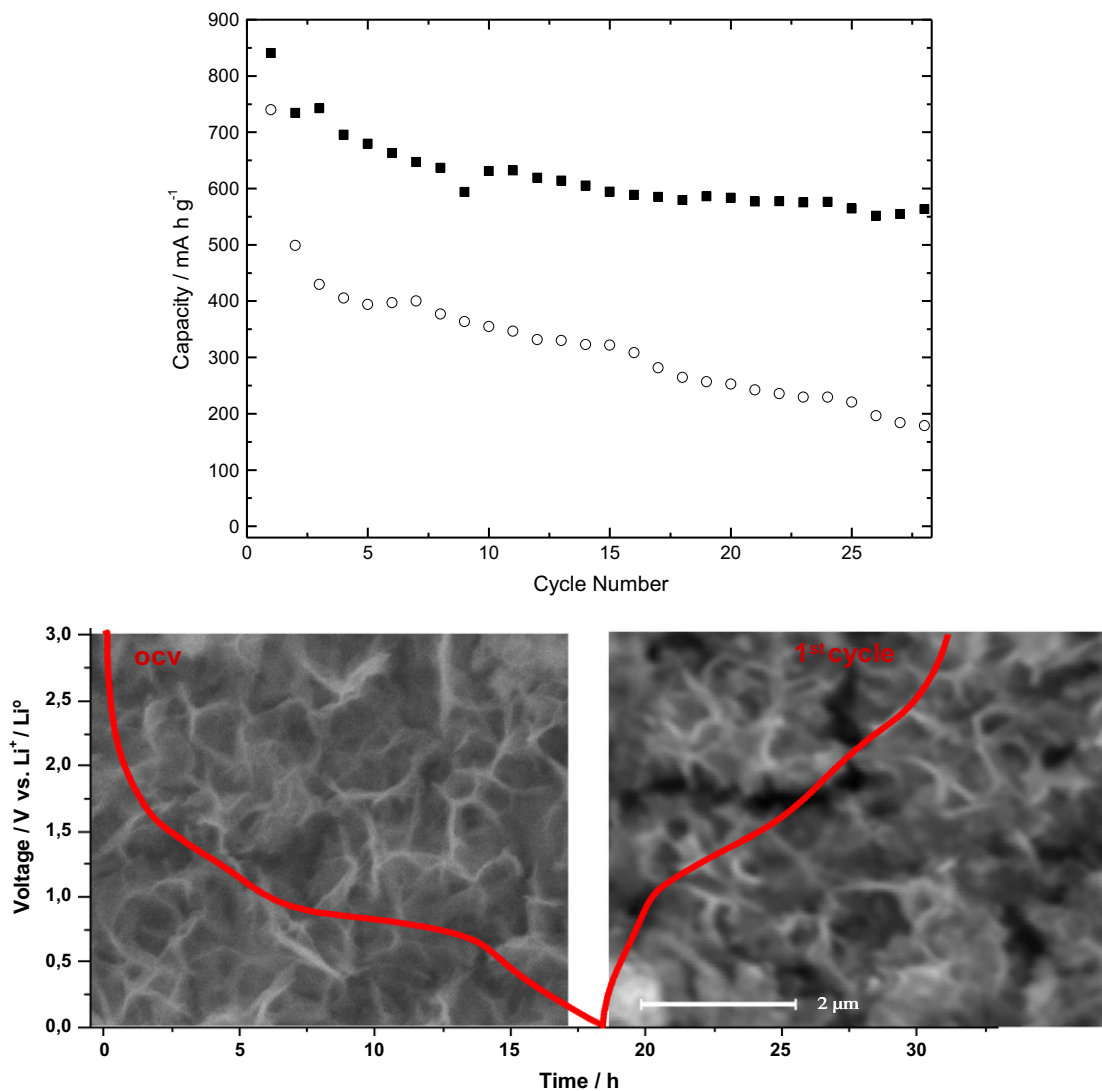


Fig. 5. Upper: cycling life study of electrodeposited-annealed FeNi-based electrodes fabricated at two different times: 240 s (filled circles) and 1200 s (hollow circles). Lower: comparison of electrodes morphology using SEM measurement before discharge (open circuit voltage) and after charge at 3.0 V of the electrodeposited FeNi-based electrodes (short deposition time = 240 s).

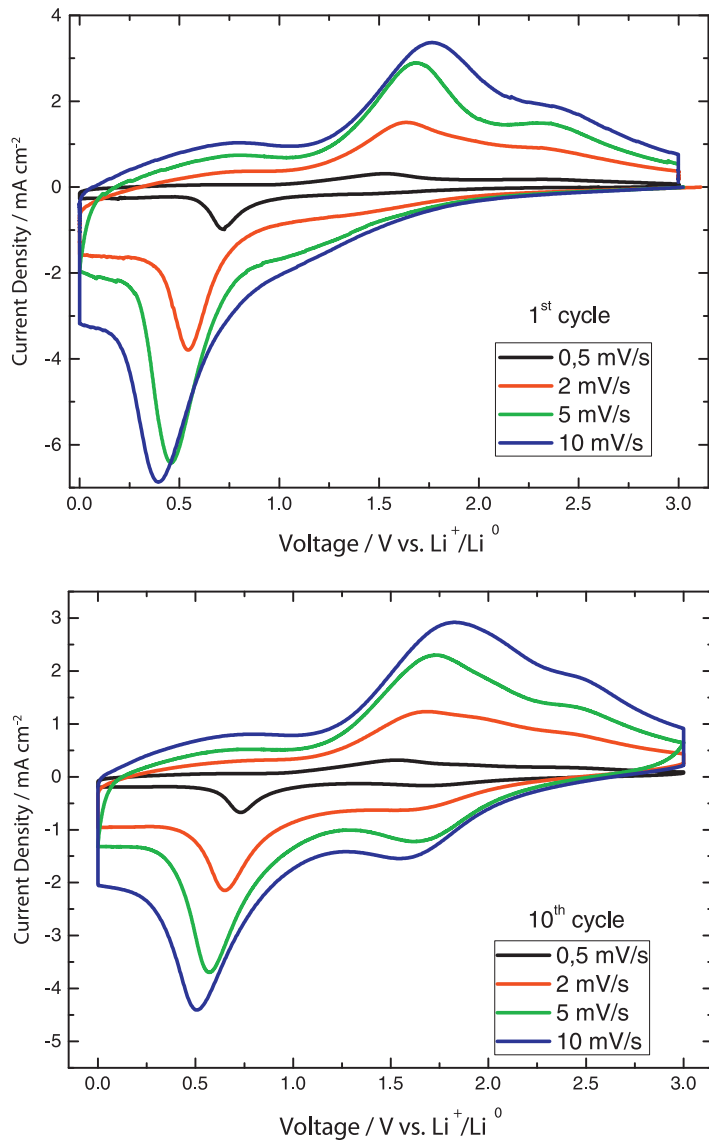


Fig. 6. Cyclic voltammetry at cycling rates in the 0.5–10 mV s⁻¹ interval.

ibility of the first cycle (ca. 85%, Fig. 4). Thus the capacity loss due to the loss of the 1.5 V band after SEI formation in the first discharge is compensated by the capacity associated to the development of the 1.8 V band in the second discharge. The origin of the latter band will be discussed in the light of the faradic/capacitive behavior.

XPS of oxidized FeNi-based electrodes after reaction with lithium were recorded (Fig. 3). After a partial lithiation (500 mA h g⁻¹) additional narrow peaks are observed at ca. 853 eV for Ni2p and 706 eV for Fe2p, which can be clearly assigned to metallic Ni and Fe, respectively. After total discharge down 0.001 V using GITT the spectra consist of a unique peak of Ni and Fe elemental, indicating the reduction of the metals had taken place (Fig. 3). These results unequivocally confirm that the conversion reaction takes place in the studied electrodes.

Changes in surface energy may have a marked impact on the experimental cell potential of the conversion reaction, as previously postulated [23]. Such effects may be responsible for the observed potential changes in the oxidized NiFe (Fig. 5). Thus a remarkable increase in surface area should not take place during electrochemical reactions with Li of the short-time sample. SEM

observations confirmed the absence of visible textural changes upon cycling in that best sample (Fig. 5). However, in nanocrystalline samples (powder [18,20] or film [6]), in which textural changes on cycling are more limited; the irreversible capacity is also large. Thus, a more plausible origin is the poorly crystallized character of the nanoparticles of the short-times sample.

The cycling experiments of the oxidized FeNi-based thin film electrodes are also shown in Fig. 5. Obviously, the areal capacities differ according to the amount of electroactive material in the electrode. Therefore, the capacity of 5-times thicker thin film displayed a capacity of 1330 μ A h cm⁻² almost 5 times higher than the thinner film (1 μ m thin film gave 295 μ A h cm⁻²). The amorphous thin film exhibited around 840 mA h g⁻¹ and partially crystalline thin film around 740 mA h g⁻¹. The corresponding capacity retention over 30 cycles is 70% and 24%, respectively.

The reasons why the oxidized FeNi (240 s) sample has better capacity retention are: (i) Low activation energy required to form the M-Li₂O aggregates, and (ii) better accessibility of Li⁺ ions to the complete mass of active material. Both properties are enhanced by the nanocrystalline thin-film character of the starting material. The 15% of irreversibility in the first cycle is due to the electrolyte

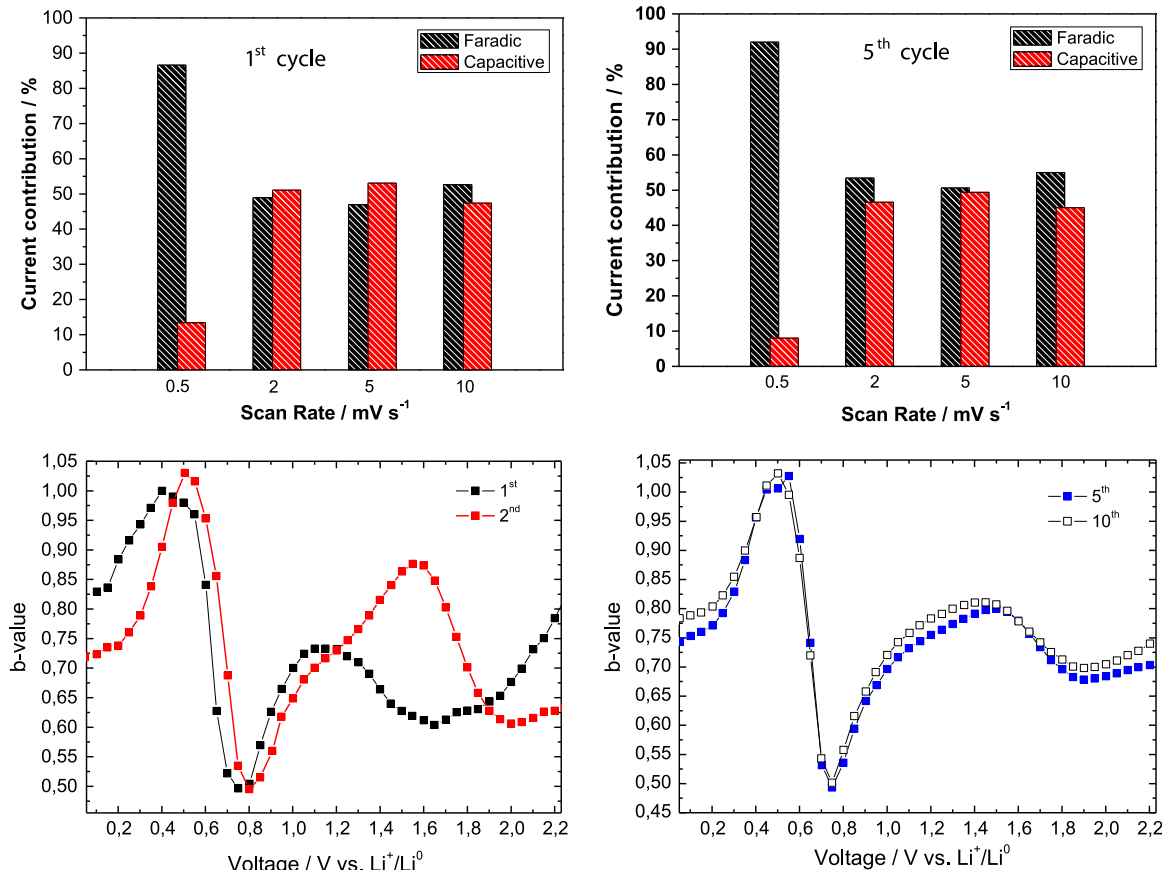


Fig. 7. Upper: comparison of total capacity storage vs. scan rate in step potential electrochemical spectroscopy discharges of electrodeposited-annealed FeNi-based electrodes (240 s) for: the first (left), and fifth (right) discharge. Lower: calculated *b*-values of electrodeposited FeNi-based electrodes film as a function of the potential (Li⁺ reaction) for: first–second (left), and fifth–tenth discharges (right).

decomposition and/or polymeric layer formation during the discharge process. Moreover, the decreased irreversibility can be also associated to the use of the electrodes free of additives such as binders (PVDF) and conductive agents (Carbon Black).

To further understand the origin of the charge storage behavior, first cycle reversibility and cycling properties of the FeNi-based electrodes, the separation of possible capacitive and conversion reaction faradic contributions to the total stored charge. For this purpose, cyclic voltammograms using different scan rates were recorded (Fig. 6). The analysis of these results allows discerning the faradic contribution due to diffusion-controlled reactions such as the conversion reaction, from the possible pseudocapacitive and double-layer contributions, that cannot be separated, according to previous literature [32–34]. Fig. 7 depicts the differences in the current distribution (total stored charge, conversion reaction and capacitance) as a function of scan rate of the first and fifth cycle. The faradic and capacitive contributions are similar when cycling at scan rates of 2, 5 and 10 mV s⁻¹ (Fig. 7). In contrast, a high faradic contribution (92–86%) is found for first and subsequent cycles solely when a slow scan rate is used (e.g. 0.5 mV s⁻¹), while the capacitive contribution around 8–14% is found.

In order to know the voltage regions that shows conversion reaction or capacitive response in the first and subsequent discharges, the slope of the $\log i$ vs. $\log v$ plots is a clear indication. This parameter, henceforth referred to as “*b*” was calculated from the cyclic voltammograms, by the method described by Brezesinski et al. [33]. The scan range used for this study is 0.5–10 mV s⁻¹. For *b* = 1, a pure capacitive contribution is assumed. For *b* = 0.5, the current is proportional to the square root of the sweep rate

and the process is identified as a faradic contribution from the conversion process. Fig. 7 shows that the process at 0.8 V is basically faradic (*b* close to 0.5) for first and subsequent discharges. The only changes observed from first to second discharge resides in the new availability to store capacity in the voltage window of around 1.40–1.75 V, because a capacitive contribution is observed in subsequent discharges (*b* ~ 0.85) that replaces the irreversible faradic response given from electrolyte decomposition. The second cycle is basically reproducible for further cycles. In order to assess the pre-eminence of faradic contribution at a low kinetic rate, an alternative method was applied, according to previous literature [35,36]. Cyclic voltammograms were recorded in the 0–1.5 mV s⁻¹ range (Fig. 8). The changes in the current intensity of the D, C1, C2 and S-peaks as a function of the square root of the scan rate were plotted in Fig. 8. The current peaks were normalized by the electrode area. The linear relationship observed in this plot evidences a faradic conversion process.

4. Conclusions

Electrochemical procedures provide new strategies to prepare electrode materials for Li-ion batteries. A preparation route of transition metal oxide films is proposed, based on the deposition of transition metal ions followed by mild thermal oxidation in air. Electrochemical results in lithium test cells showed the best behavior of a conversion electrode in terms of first-cycle columbic efficiency and polarization. Discharge capacities above 600 mA h g⁻¹ are found without using binder additives or conductive

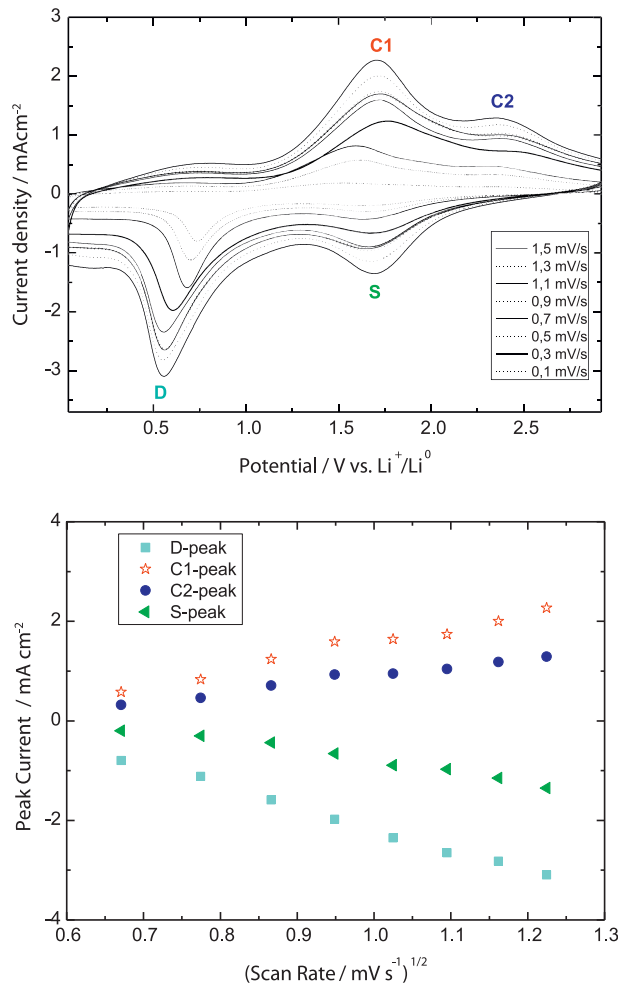


Fig. 8. Upper: cyclic voltammograms of oxidized FeNi-based electrode at different scanning rates (0.1–1.5 mV s⁻¹). Lower: normalized peak currents as a function of scan rate for D, C1, C2 and S-peaks.

agents. The improvement is ascribed to the combined nanocrystalline and thin film nature of the material [37–41]. For high cycling rates, non-faradaic contributions replace the irreversible electrolyte decomposition.

Acknowledgments

The authors are indebted to the MICINN (contract MAT2011-22753) and “Junta de Andalucía” (FQM288, contracts FQM-7206 and FQM6017). G.F. Ortiz is indebted to the ‘Ramón y Cajal’ program (RYC-2010-05596). We thank to UCO-SCAI, IUIQFN, ALISTORE-ERI, to the National Center of Electronic Microscopy from “Universidad Complutense de Madrid” for helpful assistance in the TEM study.

References

- M. Voith, C&EN 88 (2010) 24.
- N. Kamaya, K. Homma, Y. Yamakawa, M. Hirayama, R. Kanno, M. Yonemura, T. Kamiyama, Y. Kato, S. Hama, K. Kawamoto, A. Mitsui, Nat. Mater. 10 (2011) 682.
- G.F. Ortiz, I. Hanzu, T. Djenizian, P. Lavela, J.L. Tirado, P. Knauth, Chem. Mater. 21 (2009) 63.
- G.F. Ortiz, I. Hanzu, P. Knauth, P. Lavela, J.L. Tirado, T. Djenizian, Electrochim. Acta 54 (2009) 4262.
- G.F. Ortiz, I. Hanzu, P. Lavela, P. Knauth, J.L. Tirado, T. Djenizian, Chem. Mater. 22 (2010) 1926.
- G.F. Ortiz, I. Hanzu, P. Lavela, P. Knauth, J.L. Tirado, T. Djenizian, J. Mater. Chem. 20 (2010) 4041.
- G.F. Ortiz, J.L. Tirado, Electrochim. Commun. 13 (2011) 1427.
- M.C. López, G.F. Ortiz, P. Lavela, R. Alcántara, J.L. Tirado, ACS Sustainable Chem. Eng. 1 (2013) 46.
- A. Brenner, Electrodeposition of Alloys, 1, Academic Press, New York, 1963.
- K. Attenborough, R. Hart, S.J. Lane, M. Alper, W. Schwarzacher, J. Magn. Magn. Mater. 148 (1995) 335.
- M. Matlosz, J. Electrochem. Soc. 140 (1993) 2272.
- U. Lacnjevac, B.M. Jovic, V.D. Jovic, Electrochim. Acta 55 (2009) 535.
- K. Wandelt, Surf. Sci. Rep. 2 (1982) 1.
- W. Weiss, W. Ranke, Prog. Surf. Sci. 70 (2002) 1.
- A.G. Fitzgerald, G. Muir, Surf. Interface Anal. 8 (1986) 247.
- J.A. Schreifels, P.C. Maybury, W.E. Swartz, J. Catal. 65 (1980) 195.
- Y.E. Roginskaya, O. Morozova, E. Lubnin, Y.Y. Ulitina, G. Lopukhova, S. Trasatti, Langmuir 13 (1997) 4621.
- P. Poizot, S. Laruelle, S. Gruegeon, L. Dupont, J.M. Tarascon, Nature 407 (2000) 496.
- G. Binotto, D. Larcher, A.S. Prakash, R. Herrera Urbina, M.S. Hegde, J.M. Tarascon, Chem. Mater. 19 (2007) 3032.
- P. Lavela, J.L. Tirado, J. Power Sources 172 (2007) 379.
- E. Hosono, S. Fujihara, I. Honma, H. Zhou, Electrochim. Commun. 8 (2006) 284.
- C. Vidal-Abarca, P. Lavela, J.L. Tirado, J. Phys. Chem. C 114 (2010) 12828.
- J. Cabana, L. Monconduit, D. Larcher, M.R. Palacín, Adv. Mater. 22 (2010) E170.
- P. Poizot, S. Laruelle, S. Gruegeon, L. Dupont, J.M. Tarascon, J. Power Sources 97 (2001) 235.
- S. Gruegeon, S. Laruelle, R. Herrera-Urbina, L. Dupont, P. Poizot, J.M. Tarascon, J. Electrochim. Soc. 148 (2001) A285.
- X. Cheng, E. Yegan Erdem, S. Takeuchi, H. Fujita, B.D. Ratner, K.F. Bohringer, Lab Chip 10 (2010) 1079.
- S. Laruelle, S. Gruegeon, P. Poizot, M. Dollé, L. Dupont, J.M. Tarascon, J. Electrochim. Soc. 148 (2000) A627.
- P. Balaya, A.J. Bhattacharyya, J. Jamnik, Y.F. Zhukovskii, E.A. Kotomin, J. Maier, J. Power Sources 159 (2006) 171.
- J.L. Tirado, Mater. Sci. Eng., R 40 (2003) 103.
- M.F. Hassan, Z. Guo, Z. Chen, H. Liu, Mater. Res. Bull. 46 (2011) 858.
- X. Li, A. Dhanabalan, K. Bechtold, C. Wang, Electrochim. Commun. 12 (2010) 1222.
- B.E. Conway, V. Birss, J. Wojtowicz, J. Power Sources 66 (1997) 1.
- T. Brezesinski, J. Wang, J. Polleux, B. Dunn, S.H. Tolbert, J. Am. Chem. Soc. 131 (2009) 1802.
- M.J. Aragón, B. León, T. Serrano, C. Pérez-Vicente, J.L. Tirado, J. Mater. Chem. 21 (2011) 10102.
- M. Zukalova, M. Kalbáč, L. Kavan, I. Exnar, M. Graetzel, Chem. Mater. 17 (2005) 1248.
- H. Liu, Z. Bi, X.G. Sun, R.R. Unoicic, M.P. Paranthaman, S. Daí, G.M. Brown, Adv. Mater. 23 (2011) 3450.
- U.G. Nwokeke, A.V. Chadwick, R. Alcántara, M. Alfredsson, J.L. Tirado, J. Alloys Compd. 509 (2011) 3074.
- D. Wei, Electrochemical Nanofabrication: principles and applications, in: Di Wei (Ed.), Electrochemical Nanofabrications: A General Review, Pan Stanford Publishing Pte. Ltd., 2012, pp. 1–62.
- J. Zhong, X.L. Wang, X.H. Xia, C.D. Gu, J.Y. Xiang, J. Zhang, J.P. Tu, J. Alloys Compd. 509 (2011) 3889.
- Y.J. Mai, X.H. Xia, R. Chen, C.D. Gu, X.L. Wang, J.P. Tu, Electrochim. Acta 67 (2012) 73.
- M.V. Reddy, T. Yu, C.-H. Sow, Z.X. Shen, C.T. Lim, G.V. Subba Rao, B.V.R. Chowdari, Adv. Funct. Mater. 17 (2007) 2792.